

Space-based Ionosonde Receiver and Visible Limb-viewing Airglow Sensor (SIRVLAS): A CubeSat instrument suite for enhanced ionospheric charge density measurements

Sujay Swain^a, Benjamin Cohen^a, Ryan He^a, Michael Ilie^a, Ishaan Shrestha^a, Luca Zeng-Mariotti^a, Rajit Mukhopadhyay^a, Santiago Lisa^a, and Andrew Healey^a

^ablair3sat, PO Box 1084, Rockville, MD, United States of America

ABSTRACT

blair3sat is a student-run team based in Montgomery County, Maryland, developing a 3U CubeSat. The satellite will include the instrument suite SIRVLAS, which contains an optical instrument and a Radio Frequency (RF) instrument. The objective of the mission is to prove that a set of instruments like SIRVLAS in a CubeSat-style satellite is able to generate a three-dimensional mapping of ionospheric electron density. The optical instrument will measure OI 777.4 nm emissions in the lower ionosphere in a limb view geometry. Since the 777.4 nm wavelength is emitted from the radiative recombination reaction of O^+ and e^- , its intensity is proportional to the square of the electron density. Therefore, by measuring the intensity of the 777.4 nm emission, electron densities may be calculated. These electron densities will be used as a reference for the data processing of RF signals. Specifically, correlation between the two instruments is performed through constrained optimization of known ray-tracing PDEs. Mappings of electron density in the ionosphere will allow for a better understanding of radio applications including radar and missile tracking, while allowing for the verification of current atmospheric and climatological models.

Keywords: CubeSat, Optical, Ionosphere, Low Earth Orbit, Climate Change, Ionosonde, Education

1. INTRODUCTION

SIRVLAS (Space-based Ionosonde Receiver and Visible Limb-viewing Airglow Sensor) introduces a novel method of analyzing and calculating electron densities in the ionosphere by correlating ionosonde soundings with airglow measurements.

The instrument described in this paper is a secondary instrument to the satellite's primary Radio Frequency (RF) instrument and will provide a source of regularization during the computation of the charge density mapping around the satellite. The objective of the optical instrument is to take reliable measurements of the surrounding electron density concurrently with the RF instrument in order to provide reference data for correlation.

2. BLAIR3SAT

blair3sat is a non-profit 501(c)(3) subsidiary based in Montgomery County, Maryland. Founded in 2018, blair3sat is a team that is run by, and consists of, STEM-inclined high school students. For the past two years, blair3sat's members have engaged in researching optical and radio physics. blair3sat has built its reputation in the CubeSat community, reaching out to speak at schools in the Montgomery County area and at CubeSat conferences such as the 2019 Annual Small Satellite Conference. The science objectives of the mission are contextualized in an educational and professional setting, providing an intense and rewarding experience in advanced STEM topics to over 20 high school students in Montgomery County, Maryland. blair3sat aims to prove the viability of high-school CubeSat science missions.

3. BACKGROUND SCIENCE

3.1 Origins of the 777.4 nm Emission

The airglow emission of 777.4 nm is a OI quintet emission originating from the $3^5p - 3^5s$ transition of atomic oxygen. This emission is commonly used for both space and ground-based analysis of ionospheric nightglow in order to extrapolate and study atmospheric parameters and excitation mechanisms.¹⁻³

The primary source for 777.4 nm emissions is atomic oxygen radiative recombination reactions.^{2,4} This reaction is as follows:



Other than radiative recombination, two other sources have been accepted as excitation mechanisms for the emission of this wavelength during nightglow. The first source, atomic oxygen mutual neutralization, adheres the following set of reactions:⁵



However, this source has been shown to represent less than 777.4 nm 10% of emissions.¹ The second source, dissociative excitation of O_2 molecules, is near negligible, representing less than 5% of OI 777.4 nm emissions.⁶ In addition, this source is primarily emitted within the E region of the atmosphere,⁷ below the altitudes that SIRVLAS's optical instrument will measure, and therefore will likely not affect the measurements for the majority of the instrument's operation.

The 777.4 nm emission can also occur due to photo-electron impact reactions. However, these reactions only occur in day-side aurora at high altitudes.⁸ Therefore, they may also be ignored because the proposed instrumentation will only operate on the night-side.

3.2 Radiative Recombination Reactions and Electron Density

The 777.4 nm emission is essential for measuring electron density because its primary source is radiative recombination. As seen in the radiative recombination reaction in Equation 1, the volume emission rate of 777.4 nm emissions is proportional to electron density and to the density of O^+ ions, with a small contribution from mutual neutralization. This equation shows that:⁴

$$V_{777.4} = \alpha_{777.4}[O^+][e^-] + \frac{\beta_{777.4}k_1k_2[O][O^+][e^-]}{k_2[O^+] + k_3[O]} \quad (4)$$

where $V_{777.4}$ is the volume emission rate, $\alpha_{777.4}$ is the partial rate coefficient for radiative recombination, and $\beta_{777.4}$, k_1 , k_2 , and k_3 are rate coefficients. The values of these coefficients used in this work are given in Table 1.⁹

Table of Rate Coefficients	
Coefficient	Value
$\alpha_{777.4}$	$7.8 \times 10^{-13} cm^3 s^{-1}$
k_1	$1.3 \times 10^{-15} cm^3 s^{-1}$
k_2	$1.5 \times 10^{-7} cm^3 s^{-1}$
k_3	$1.4 \times 10^{-7} cm^3 s^{-1}$
$\beta_{777.4}$	$0.42 cm^3 s^{-1}$

Table 1. Rate coefficients used in Equation 4.

From this equation, one may determine a relationship between emissions and the electron density itself through the common assumption that the concentration of O^+ is approximately equal to the concentration of e^- in the lower ionosphere.^{1,4,9} Therefore, the equation becomes:

$$V_{777.4} = \alpha_{777.4}[e^-]^2 + \frac{\beta_{777.4}k_1k_2[O][e^-]^2}{k_2[e^-] + k_3[O]} \quad (5)$$

On inspection of this equation, one will note that the two sources of the 777.4 nm emission, radiative recombination and mutual neutralization, are respectively represented within the first and second terms. Thus, in order to extract the electron density from the emission of 777.4 nm, one must remove or account for the contamination due to mutual neutralization. There are two methods to do this. First, one could assume that the emissions emanating from mutual neutralization make up a percentage of the emissions.⁹ This procedure would leave the equation as:

$$V_{777.4} = \frac{\alpha_{777.4}}{1-p}[e^-]^2 \quad (6)$$

where p is the fraction of emissions caused by mutual neutralization. In this equation, a proportional relationship is evident between the square of the electron density and the volume emission rate. A second approach would be to include neutral oxygen concentrations within the forward model. This method is discussed later in Section 5.2.

4. INSTRUMENT DESIGN

Due to constraints on SIRVLAS' RF instrument, the satellite is only able to take measurements in very low Earth orbit (VLEO). Specifically, the satellite instrumentation will be operating within the altitudes of 200 km to 300 km as the satellite's orbit decays. The 777.4 nm emission peaks at around 350 km but is emitted as low as 150km.¹⁰ As a result, emissions originating at distances ranging from adjacent to the satellite all the way to the end of the limb must be considered. For each emission, the specific limb it originated within must be derived. In other words, the instrument must be able to make a limb scan while located within the emitting region itself. The proposed general optical instrument design and processing methods to take these measurements is covered in Section 4.1, while certain specifics regarding aspects of that design are described in the subsequent sections.

4.1 Instrument Geometry and Concept

As discussed in Section 4, the instrument must be able to measure emissions from a large range of distances from the satellite while still taking a high resolution limb scan of the lower ionosphere. This task is done through the utilization of processing methods as well as instrument geometry to narrow down where the emission must have originated from.

First, consider the instrument pictured in Figure 1. This design only contains a vertical detector array, e.g. a charge-coupled device (CCD), within an opaque box with an aperture. In this situation and for the overall design of the instrument, the aperture is assumed to be rectangular and therefore is defined by a width and height. This hole would be cut out from within a circular shutter, if need be. If the Fields of View (FOVs) of two pixels on this array, pixels A and B , are constructed, then it is possible to define three regions of space. Region 1 ($R(1)$) is the region from which light emissions may reach pixel B but not pixel A . Region 2 ($R(2)$) is the region from which light emissions may reach either pixel A or pixel B . Finally, Region 3 ($R(3)$) defines the region from which light emissions may only reach pixel A . One may then write the following:

$$A_I = R(3) + R(2) \quad (7)$$

$$B_I = R(1) + R(2) \quad (8)$$

where A_I is the reading of pixel A , and B_I is the reading of pixel B . Therefore, it becomes evident that the difference between these two pixels may be described as:

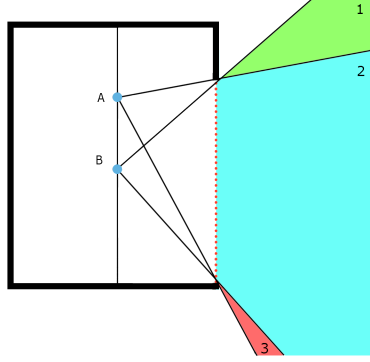


Figure 1. Simple instrument with a vertical detector array, 2 example pixels, and corresponding FOVs. Note how the different FOVs create 3 distinct regions.

$$B_I - A_I = R(1) - R(3) \quad (9)$$

As the size of $R(3)$ is minimized, this subtraction approaches defining $R(1)$. Although one could minimize $R(3)$ by decreasing the length of \overline{AB} , this method is dependent on the resolution of the detector and still will not completely eliminate $R(3)$. A superior method is shown in Figure 2, where the detector is angled such that the lower FOV lines that define $R(3)$ are constrained not by the location of the pixel on the detector and the lower lip of the aperture, but by the detector itself. Therefore, the lower FOV lines are defined in the same way for any pixel on the detector and $R(3)$ is completely eliminated from the situation. Now, the difference between the pixels' measurements, $B_I - A_I$, is equal to $R(1)$.

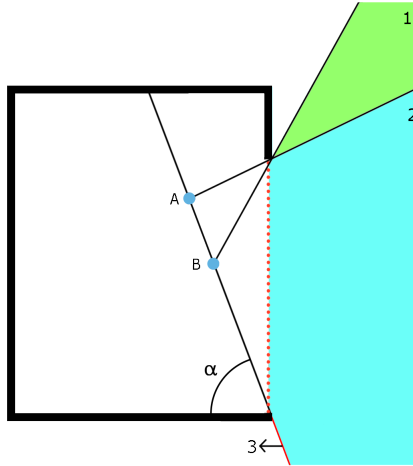


Figure 2. Instrument with a slanted detector array, 2 example pixels, and corresponding FOVs. Note how the different FOVs create 2 distinct regions and remove $R(3)$.

To include the filter setup and the shutter required for this instrument, the detector is shifted back to be co-linear with a diagonal ray from the bottom-most point on the aperture, as seen in Figure 3. In this figure, the purple section represents the filter setup while the yellow section represents an aperture defined by the shutter.

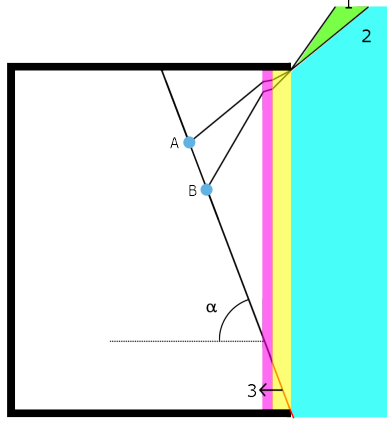


Figure 3. Complete instrument setup with a slanted detector array, 2 example pixels, a shutter (yellow), and a filter (purple).

This setup's geometry allows for the definition of an intensity measurement for the thin $R(1)$ by subtracting the results of two adjacent pixels on the detector. One may also note that a scan is easily completed by choosing points in different places upon the detector.

This process makes the inherent assumption that incident light upon the instrument is treated equally regardless of its angle of incidence (AOI), as the process assumes that $R_A(2) = R_B(2)$ or, in other words, the space overlapped by the FOV of two pixels is treated equally by both pixels. The consequences of this assumption upon the design process of the instrument is discussed in detail within Sections 4.3 and 4.4.

4.2 Specific FOV Calculations

The FOV of the instrument may be calculated through the instrument's geometry. As shown in Figure 4, the angle of the upper vertical FOV line from the horizontal given a point on the detector may be written as:

$$0 = \tan(\theta)(p \cos(\alpha) + w) + (p - L_d) \sin(\alpha) + d \left(\frac{\sin(\theta)}{\sqrt{n^2 - \sin(\theta)^2}} \right) \quad (10)$$

where w is the distance between the filter and the aperture, L_d is the length of the detector, α is the angle of the detector, d is the width of the filter, and n is the index of refraction of the filter. θ is the angle between the upper vertical FOV line from the point and the horizontal (as seen in Figure 4). This equation yields infinitely many solutions for θ and therefore it must also be stated that θ is bound in the range $[0, \pi/2]$ radians, from which it may be further constrained by instrument geometry.

In this equation, α may vary depending on the specific design. However, it is optimal to maximize α as that also maximizes the angular range of the scan. The maximum α may be defined by the following equation:

$$S_h = w \tan(\alpha) + d \frac{\sin(\alpha)}{\sqrt{n^2 - \sin(\alpha)^2}} + L_d \sin(\alpha) \quad (11)$$

where S_h is the height of the aperture.

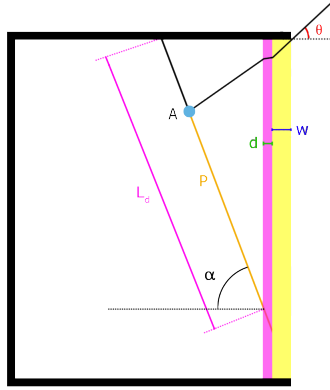


Figure 4. A diagram with the variables used for FOV calculations.

From this equation, we may calculate the vertical angle defining $R(1)$ by taking the difference between θ for two pixels on the detector that are Δp from each other. One may note that this $\Delta\theta$ is not only dependent on Δp but also on the p for one of the pixels (as the p for the other pixel may be expressed as: $p_A = p_B + \Delta p$). Therefore, the vertical resolution will change slightly over the scan. This effect may be seen within Figure 5, where $\Delta\theta$ is shown for the entire detector with two different Δp using the instrument parameters described below. It is worth noting that, within the processing of the instrument data, the limb scan may be calculated for multiple values of Δp . Therefore, the instrument is effectively taking a limb scan of many different vertical FOVs concurrently. These scans of different vertical FOV may be compared during processing. The changing vertical FOV over the scan is not problematic because it is accounted for within the retrieval process.

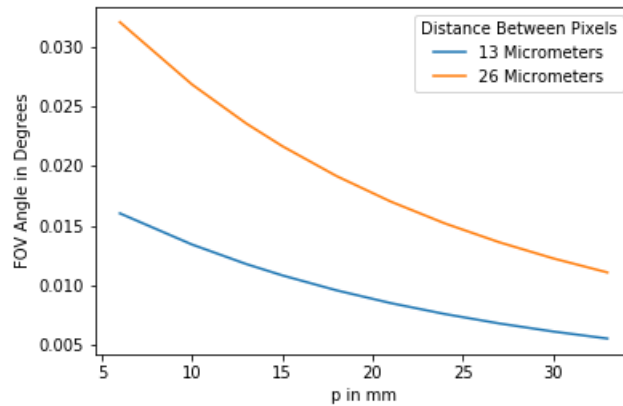


Figure 5. The vertical FOV defining $R(1)$ versus the p of the pixel with the smaller p value. This FOV is shown with two values of Δp .

Because this project is still within the research and development phase and specific components have not been selected it, is not possible to calculate the exact FOV of the final instrument. However, one may approximate the

vertical FOV to be, between two adjacent points on the detector ($\Delta p = 0.013$), 0.016° (rounded to the nearest thousandth of a degree). This value is calculated by assuming an aperture height of 25mm, a distance between the aperture and the filter of 23mm (calculated assuming 1.5mm between the shutter and the filter and a shutter thickness of 21.5mm), a filter width of 3mm, a filter with an index of refraction of 1.5, a detector length of 35mm, an α of 0.41 radians (which is the maximum for the instrument parameters rounded to two decimal places), a p of 6mm, and a Δp of 0.013mm.

Table of Instrument Parameters		
Variable	Description	Hypothetical Value
S_h	Height of the aperture	25 mm
S_w	Width of the aperture	2 mm
p	Distance up the detector	6 mm
Δp	Distance between pixels	0.013 mm
w	Distance between filter and aperture	23 mm
L_d	Detector length	35 mm
α	Detector angle	0.41 rad
d	Filter width	3 mm
n	Filter index of refraction	1.5

Table 2. List of instrument parameters, brief descriptions, and hypothetical values necessary for Equations 10 and 12.

In order to fully understand the abilities of the proposed instrument, one must also compute the horizontal FOV. This value changes depending on p as well as the direction one is looking out the aperture. However, because the pixels are so close together, their horizontal FOV's may be assumed to approximately line up. Therefore, it is a good diagnostic of the instrument's ability to calculate the horizontal FOV of the upper defining line of $R(1)$ because that value is approximately the horizontal FOV of the entirety of $R(1)$ and therefore the horizontal FOV of the limb scan. This definition will be used for the remainder of this work and may be calculated similarly to the vertical FOV through:

$$\frac{S_w}{2} = \tan\left(\frac{1}{2}\phi\right) \frac{p \cos(\alpha) + w}{\cos(\theta)} + \frac{nd \sin(\frac{1}{2}\phi)}{\sqrt{(n^2 - \sin(\theta)^2)(n^2 - \sin(\frac{1}{2}\phi)^2)}} \quad (12)$$

where ϕ is the horizontal FOV and using the same notations as above with S_w representing the width of the instrument's aperture. Assuming the same parameters as for the calculations of the vertical FOV, but with the addition of an aperture width of 2mm, the horizontal FOV is 3.52° (rounded to the nearest hundredth). The range of horizontal FOVs for this hypothetical setup is shown in Figure 6.

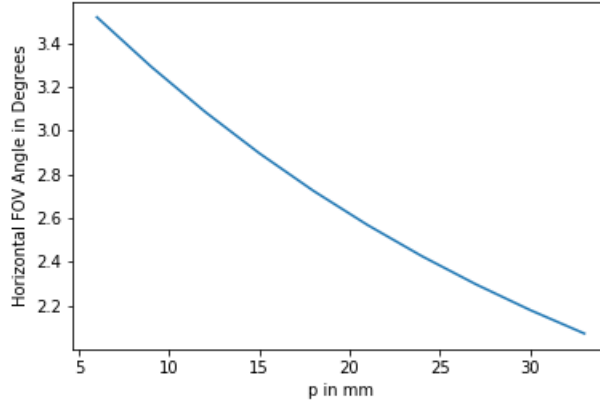


Figure 6. The horizontal FOV versus the P of the pixel with the smaller p value.

4.3 Filters

Due to the presence of ionospheric emissions of multiple wavelengths within the Earth's nightglow, many of which are within the detection range of a CCD, a high quality filter is required to ensure accurate measurements. The filter is placed in front of the CCD to constrain the measurements to the 777.4 nm emission as shown in Figure 3.

A standard bandpass filter would have been the ideal solution. However, light must be filtered equally regardless of the AOI and the passband shift of bandpass filters depending on the AOI of incident light prevents them from doing this effectively.

Since the passband shift prevents the use of a standard bandpass filters, a filter setup consisting of a colored glass absorptive filter will be implemented instead. Although these filters typically have a wider passband than more standard, layered bandpass filters, they are much more resistant to passband shift caused by high angles of incidence.

4.4 Charge-Coupled Device and the Angle of Incidence

A CCD is a type of detector commonly used within imaging applications due to its fast response speed and high resolution. It is well suited for this instrument as the resolution of the scan is directly related to the resolution of the detector.

One issue is that the CCD's response to light varies based on the AOI. This change in detector responsivity creates two potential sources of error within the data processing .

The first error is a scaling upon the light arriving from $R(1)$. This effect may be severe if not accounted for. However, due to the nature of the instrument, this source of error may be somewhat corrected. Begin by considering a ray of light traveling from some point within $R(1)$ to pixel B.

One bound of the AOI (from the normal to the pixel) is equivalent to the angle of the top FOV line from pixel B (or the angle between \overline{BP} and the detector as shown in Figure 7). The other bound is found as point H is placed upon the upper FOV line of pixel A (and the second defining line of $R(1)$, as shown in Figure 7) and moved out toward infinity. As point H travels farther and farther from the instrument, line \overline{BH} approaches parallel to \overline{AH} . Therefore, the second bound upon the AOI is the angle between \overline{AH} and the detector. Following from these bounds, the range of possible AOIs of \overline{BH} is the size of the defining angle of $R(1)$ from the AOI of \overline{BP} to the AOI of \overline{AH} .

To correct for this scaling, it is an adequate assumption to divide out the cosine of the angle of line \overline{BP} . This is an acceptable procedure because of the small size of $R(1)$ and the corresponding small range of AOIs possible from an emitter in that region.

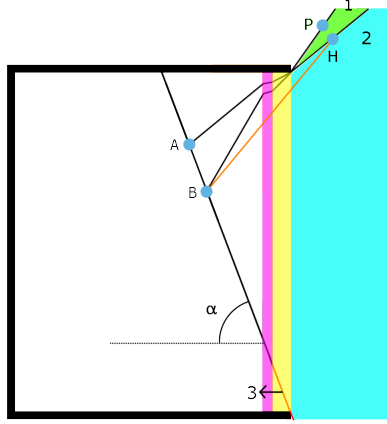


Figure 7. Complete instrument with example emitter point H in $R(1)$.

The other error caused by changes in CCD responsiveness due to the AOI is not so easy to solve and is problematic within the subtraction phase of processing. As described in the end of Section 4.1, the process requires $R(2)$ to be treated equally for both pixels, as only then does $R_A(2)$ cancel $R_B(2)$ completely and leave only $R(1)$. However, this condition is no longer the case. As shown in Figure 8, the light emitted from some point F in $R(2)$ strikes pixels A and B with a slightly different AOI and therefore is treated slightly different by the two pixels. Unlike the first source of error described in this section, the range of AOIs possible from points within $R(2)$ is fairly large, and this effect cannot be easily accounted for. However, due to the instrument geometry, this error is negligible.

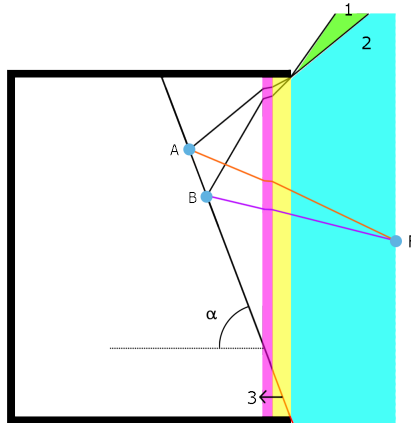


Figure 8. Complete instrument with example point F in $R(2)$.

As mentioned above, the pixels on the CCD are incredibly close together, on the range of a few micrometers.

Any point outside the shutter and filters is already very far away from the pixels relative to the distance between each other. Thus, the difference in AOI between the two pixels will be very small for that point and, after the subtraction step, the effect will not significantly impact the results. However, it is worth noting that the effect sums over all of the emissions within $R(2)$.

5. RETRIEVAL

The proposed instrument will be able to take measurements along the Earth's limb with a high vertical resolution. However, it is another challenge to transform these limb measurements into suitable readings of charge density. As visualized in Figure 9, a single limb view is defined by some angle θ from the instrument's tangent line to the Earth and stretches across numerous slices of the atmosphere (denoted here L_1 , L_2 , and so on).

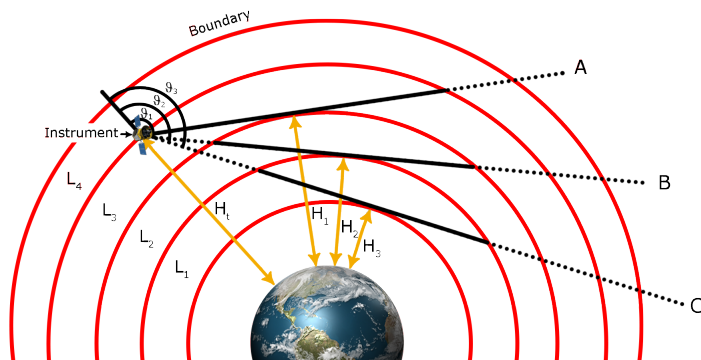


Figure 9. Image of satellite above the Earth and different limb views.

With each measurement upon the limb, emissions from a wide range of altitudes will reach the detector and become indistinguishable from emissions originating from a different region or altitude. It is inaccurate to assume homogeneity along the entire limb, so the limb view leaves the user with an inherently difficult inverse problem, in which they must use the measurements to calculate the altitude profiles of the emissions.

Within this work, another method is used which allows for an accurate solution to this inverse problem. This solution is called the Global-fit Approach¹¹ and has been used on numerous occasions since its inception.^{12–14} Section 5.1 of this paper briefly describes this approach and Sections 5.2 and 5.3 provide details about the implementation for the algorithm, such as the forward model and inverse methodology.

5.1 Global-Fit Approach

The Global-fit Approach is a non-linear least squares technique that simultaneously fits a complete limb scan. The method accounts for the fact that, within a single scan, regions within the same altitude are viewed more than once. For example, note that in Figure 9, the limb measurement A is able to capture emissions from only L_3 and L_4 . However, measurement B is not only able to also capture emissions from L_4 and L_3 , but L_2 as well. As this cycle continues, each measurement contains information regarding the other measurements above it. Therefore, the objective of the fit is to minimize a function F :

$$F(p_1, p_2, p_3, \dots, p_k) = \sum_{J=1}^M [B_J^m - B_J^c(p_1, p_2, p_3, \dots, p_k)]^2 \quad (13)$$

where M is the number of measurements, B_J^m is the J th measurement, and $B_J^c(p_1, p_2, p_3, \dots, p_k)$ is the simulated J th measurement given some atmospheric state defined by parameters $p_1, p_2, p_3, \dots, p_k$.¹¹ Such a fit has been shown to produce more accurate results than an iterative approach and is able to better account for systematic errors.¹¹ However, this approach begs two questions. First, which method is used for the minimization of F ? Second, what is the function B_J^c , henceforth referred to as the forward model?

5.2 Forward Model

An accurate retrieval system requires an accurate forward model that is able to compute what the instrument should see given a state of the atmosphere. There are two primary components in a forward model, the emission rate and the radiative transfer model.

Volume emission rate calculations are performed following the equations given in Section 3.2. Equation 5 describes the two sources of 777.4 nm emissions in F-region nightglow, radiative recombination of O^+ ions and atomic oxygen mutual neutralization. To translate these equations into ones applicable for a forward model, it must first be noted that:

$$I = \int V(z)dz \quad (14)$$

Where I is the observed intensity, z is the altitude, and $V(z)$ is the volume emission rate at that altitude.⁹ Therefore, we may rewrite equations 5 and 6 as:

$$I_{777.4} = \int (\alpha_{777.4}([e^-](z))^2 + \frac{\beta_{777.4}k_1k_2[O](z)([e^-](z))^2}{k_2[e^-](z) + k_3[O](z)})dz \quad (15)$$

and

$$I_{777.4} = \frac{\alpha_{777.4}}{1-p} \int ([e^-](z))^2 dz \quad (16)$$

As described in Section 3.2, there are two methods to incorporate mutual neutralization into the measurements. The first is to make an assumption that mutual neutralization only makes up a certain fraction of measurements. This possibility is described within Equation 16. The other possibility is to include neutral oxygen concentrations within the forward model. This means that the atmospheric state vector would include both $[O^+]$ concentrations and $[O]$ concentrations. Although this would allow the algorithm to calculate $[O]$ concentrations as well as the intensity of mutual neutralization emissions, this extra variable substantially increases the size of the search space for the minimization algorithm and therefore increases the difficulty of the minimization problem as well as the computation time required to converge upon a global minimum. While processing the data, both techniques will be used and compared.

The second aspect of the forward model is radiative transfer correction. Radiative transfer modeling attempts to correct for effects that change the intensity of the radiation as it travels and is normally composed of a combination of scattering and absorption corrective procedures. However, because 777.4 nm is a quintet emission, the lower atmosphere may be treated as optically thin and, therefore, radiative transfer correction is not necessary.¹ Since the forward model will not include radiative transfer correction, it will not be discussed here. For a detailed description of radiative transfer corrective procedures, see previous studies.⁵

5.3 Minimization Algorithm and Regularization

In order to fit a hypothetical atmospheric state to the data, a quick redefinition of F is in order as:

$$F(x) = (B_c(x) - B_m)^T S_\epsilon^{-1} (B_c(x) - B_m) + (x - x_a)^T S_a^{-1} (x - x_a) \quad (17)$$

where x is the proposed state of the atmosphere, B_c is the forward model, B_m is the collection of measurements, S_ϵ is a weighting matrix which dictates the measurements' impacts upon the cost depending on their error, x_a is the a priori state matrix used for regularization, S_a is the covariance matrix for the a priori state, and T is the transpose operation.¹⁵ This equation is used above the one described under Section 5.1 because it provides a source of regularization and produces meaningful solutions.¹⁵

In order to minimize this equation, Newton type methods are used. In such a method, the minimums of F are calculated by finding the roots of F' , in turn found through the following iterative approach:

$$x_{i+1} = x_i - F''(x_i)^{-1} F'(x_i) \quad (18)$$

which may be rewritten as:

$$x_{i+1} = x_i - (S_a^{-1} + B'_c(x_i)^T S_\epsilon^{-1} B'_c(x_i))^{-1} (S_a^{-1} (x_i - x_a) + B'_c(x_i)^T S_\epsilon^{-1} (B_c(x_i) - B_m)) \quad (19)$$

In this work, the Levenberg-Marquardt algorithm, a modification of the Gauss-Newton algorithm, is used. This algorithm provides a positive definite matrix into the F'' approximation which forces the system to be reasonably well conditioned without rank-deficiency.¹⁵ In this algorithm, the iteration equation is written as:

$$x_{i+1} = x_i - (S_a^{-1} + B'_c(x_i)^T S_\epsilon^{-1} B'_c(x_i) + \lambda_i I_n)^{-1} (S_a^{-1} (x_i - x_a) + B'_c(x_i)^T S_\epsilon^{-1} (B_c(x_i) - B_m)) \quad (20)$$

where λ_i is a rate parameter which must be set upon each iteration. A common heuristic used to set λ_i is that, with a decrease in the cost function F , λ_i is reduced by a factor of 10. On the other hand, if F is not reduced in an iteration, λ_i is increased by a factor of 10.¹⁵ This method allows the Levenberg-Marquardt algorithm to converge upon a minimum while providing a regularization term to the cost function.

The regularization covariance matrix S_a and a priori constraint x_a are defined through Tikhonov regularization. Tikhonov regularization is able to impose smoothness along specified dimensions in order to better fit to the smooth nature of the atmosphere. When Tikhonov regularization is used with the Levenberg-Marquardt algorithm, the system will converge.¹⁵

6. CONCLUSION

A methodology and optical instrument design are presented in order to take measurements of electron density in the lower ionosphere as part of the SIRVLAS instrumentation. OI 777.4 nm is detected primarily from atomic oxygen radiative recombination reactions and is consequently roughly proportional to the square of the electron density. Utilizing this relationship, an instrument design is described that is able to take limb measurements at a high vertical resolution while stationed within the emitting body. Therefore, a retrieval algorithm is applied for solving the inverse problem of finding an altitude profile given the limb scan gathered by the instrument. Although blair3sat is yet to produce a specific parts list to implement the SIRVLAS optical instrumentation, initial calculations imply the potential for further simulation and analysis. Even then, the preliminary findings yield promising findings that indicate that this design can be effective in a system of this size.

Acknowledgements

We would like to acknowledge all the people and organizations that have helped us along our path to write this paper and prepare for launch. First, we would like to thank our mentors for guiding us along our research process. Secondly, we would like thank all the scientists and companies that we contacted while searching for information related to this work. Finally, we would like to thank all current and past members of blair3sat that have made this work possible.

References

- [1] Slanger, T. G., Cosby, P. C., and Huestis, D. L., “Oxygen atom rydberg emission in the equatorial ionosphere from radiative recombination,” *Journal of Geophysical Research* **109** (2004).
- [2] Sahai, Y., Bittencourt, J. A., Teixeira, N. R., and Takahashi, H., “Simultaneous observations of oi 7774-a and [oi] 6300 a emissions and correlative study with ionospheric parameters,” *Journal of Geophysical Research* **86**(A5), 3657–3660 (1981).
- [3] Meléndez-Alvira, D. J., Meier, R. R., Feldman, J. M. P. P. D., and McLaughlin, B. M., “Analysis of the oxygen nightglow measured by the hopkins ultraviolet telescope: Implications for ionospheric partial radiative recombination rate coefficients,” *Journal of Geophysical Research* **104**(A7), 14901–14913 (1999).
- [4] Tinsley, B. A., Christensen, A. B., Bittencourt, J., Gouveia, H., Angreji, P. D., and Takahashi, H., “Excitation of oxygen permitted line emissions in the tropical nightglow,” *Journal of Geophysical Research* **78**(7) (1973).

- [5] Qin, J., Makela, J. J., Kamalabadi, F., and Meier, R. R., “Radiative transfer modeling of the oi 135.6 nm emission in the nighttime ionosphere,” *Journal of Geophysical Research: Space Physics* **120**, 10,116–10,135 (2015).
- [6] Christensen, A. B., Rees, M. H., Romick, G. J., and Sivjee, G. G., “O i (7774 Å) and o i (8446 Å) emissions in aurora,” *Journal of Geophysical Research* **83**(A4), 1421–1425 (1978).
- [7] Oyama, S.-I., Tsuda, T. T., Hosokawa, K., Ogawa, Y., Miyoshi, Y., Kurita, S., Kero, A. E., Fujii, R., Tanaka, Y., Mizuno, A., Kawabata, T., Gustavsson, B., and Leyser, T., “Auroral molecular-emission effects on the atomic oxygen line at 777.4 nm,” *Earth Planets and Space* **70**(166) (2018).
- [8] Hecht, J. H., Christensen, A. B., and Pranke, J. B., “High-resolution auroral observations of the oi(7774) and oi(8446) multiplets,” *Geophysical Research Letters* **12**(9), 605–608 (1985).
- [9] Makela, J. J., Kelley, M. C., González, S. A., Aponte, N., and McCoy, R. P., “Ionospheric topography maps using multiple-wavelength all-sky images,” *Journal of Geophysical Research* **106**(A12), 29161 – 29174 (2001).
- [10] YongMei, W. H. . W., “Airglow simulation based on the atmospheric ultraviolet radiance integrated code of 2012,” *Science China Earth Sciences* **59**(2), 425–435 (2015).
- [11] Carlotti, M., “Global-fit approach to the analysis of limb-scanning atmospheric measurements,” *Applied Optics* **27**(15), 3250 – 3254 (1988).
- [12] Clercq, C. D. and Lambert, J.-C., “A forward model of limb infrared emission spectra in a two-dimensional atmosphere,” *European Space Agency, (Special Publication) ESA SP* (07 2006).
- [13] Dinelli, B., Adriani, A., Mura, A., Altieri, F., Migliorini, A., and Moriconi, M., “Juno/jiram’s view of jupiter’s h3+ emissions,” *Philisophical Transactions of the Royal Society A* **377** (2019).
- [14] “New sciamachy handbook - earth online,” *ESA* .
- [15] Ungermann, J., [*Tomographic reconstruction of atmospheric volumes from infrared limb-imager measurements*], Forschungszentrum Jülich (2011).